

Research

Low binder content bricks: a regolith-based solution for sustainable surface construction on the Moon

Roberto Torre¹ · Aidan Cowley¹ · Carlo Giovanni Ferro²

Received: 17 November 2023 / Accepted: 6 February 2024

Published online: 22 February 2024

© The Author(s) 2024 [OPEN](#)

Abstract

This work proposes a composite construction material made by a blend of lunar regolith and thermoplastic binders in dry powder form. This solution offers advantages over regolith sintering or melting by requiring lower power consumption and simplifying the manufacturing process. However, its sustainability depends on minimizing the content of the binder material. Drawing from validated concepts used on Earth, such as polymeric concrete and compressed Earth bricks, this paper suggests that binder optimization can be achieved by simplifying and streamlining the manufacturing process, targeting parts with predefined shapes. Standardized elements like bricks or tiles ease production and assembly automation, especially when incorporating interlocking features, simplifying the payload concept transition. After drafting the process with a minimum number of basic steps, this work studies the effects of some process parameters to minimize the weight percentage of the matrix while maintaining reasonable mechanical properties. The compressive and the flexural strength are the targets of an orthogonal array Design of Experiment. Through comparison with reference values for civil engineering, the process demonstrates promising results within an organic phase as low as 10 wt%.

Article Highlights

- A manufacturing process easily scalable to larger-sized products is proposed for a regolith-rich composite material.
- Adjusting the binder weight percentage, compaction pressure, and regolith grain size improves the mechanical properties.
- A minimal binder allows for reaching possible compression and flexural strength requirements for lunar construction.

Keywords ISRU · Lunar regolith · Thermoplastic · Moon · Concrete · Bricks

1 Introduction

As we venture deeper into space exploration, the In Situ Resource Utilization (ISRU) concept has emerged as a key strategy for sustainable and self-sufficient operations beyond Earth. ISRU refers to utilizing materials available at the mission site rather than relying on imports from Earth [1], thus reducing costs and logistical challenges. When applied to lunar missions, ISRU involves extracting and processing raw materials on its surface to create resources:

✉ Roberto Torre, roberto.torre@esa.int; Aidan Cowley, aidan.cowley@esa.int; Carlo Giovanni Ferro, carlo.ferro@polito.it | ¹European Astronaut Centre, ESA, Cologne, Germany. ²Department of Mechanical and Aerospace Engineering, Politecnico di Torino, Torino, Italy.



construction materials, fuel, oxygen, and water [2]. Additionally, developing ISRU technologies and processes on the Moon serves as a blueprint for future missions to other celestial bodies [3]. The Moon is rich in valuable resources, especially regolith, a superficial layer of loose rocks, dust, and soil [4, 5]. Through different technologies, regolith can be processed and used as a construction material [6]; oxygen and minerals can also be extracted and used [7]. Additionally, the water ice deposits in permanently shadowed regions could be extracted and purified to provide resources for life support systems and fuel production [8].

Researchers have been exploring different processing methods to transform regolith into functional materials for construction and manufacturing [9]. Some of these approaches, often referred to as aggregate bonding, involve incorporating additional materials (additives or binders) to enhance the cohesion and strength of the parts [10] and enable the creation of complex shapes and designs. Binders can be organic or inorganic substances. Further approaches avoid external materials and rely on the inherent properties of the particles to partially or fully bind to each other under specific conditions. They typically involve subjecting the raw material to heat treatments, such as sintering or melting, to merge the particles [11]. This minimizes (or eliminates) the need for additional materials; however, it requires substantial energy to achieve the high temperatures needed [12]. Concentrated solar energy and microwave heating have been proposed as an alternative [13, 14], but they need sophisticated control systems [15] and precise thermal regulation [16]. Particle size distribution, composition, and mineralogy can significantly impact the outcome of these processes [17]. Those techniques can be time-consuming; achieving complete melting or adequate sintering may require extended heating periods [18], impacting manufacturing efficiency and productivity. In addition, post-treatment may be needed to enhance the properties of the products.

In the context of aggregate bonding, several approaches worth exploring, most of them in the frame of additive manufacturing. One is inspired by the Cement Contour Crafting (CCC) method, which utilizes automated feedstock supply modules for regolith powder and a liquid binder [19]. It offers a promising level of autonomy for in-situ construction [20] and excellent mechanical properties, with compressive strengths up to 48 MPa. However, it requires about 35 wt% of consumables. Additionally, the possibility of using locally mined sulfur as a co-binder is limited by its low melting temperature, which challenges its broader application across the lunar surface [21]. Operating on the Binder Jet principle, the D-shaping process has been suggested to create large-scale objects [22]: a nozzle head with 300 nozzles releases a saturated salt solution in H₂O, reacting with the MgO in the regolith. To create sufficient binding, the binder and an additional MgO added to the regolith result in consumables account for approximately 25 wt%. The material exhibited good compressive strength (17–20 MPa) and flexural strength between 1.5 and 3.5 MPa. However, violent outgassing occurred when the binder was injected in a vacuum, resulting in empty and porous structures [23]. Taylor et al. [24] achieved comparable compressive strengths through a direct material extrusion method utilizing a slurry formulation. The authors combined 74 vol% of sieved JSC-1A regolith simulant (fraction size less than 50 μm) with 26 vol% of an organic solution. Thermal debinding and sintering were necessary at the end of the process to achieve appropriate mechanical properties. A similar approach, but closer to Ink Jetting, was proposed by Jakus et al. [25] by mixing Lunar and Martian regolith simulants with elastomeric binders and a solvent mixture. The resulting ink comprised around 70–75 vol% of simulant; the authors devised a recycling strategy for the ink components to restore the crucial solvent and binder organic compounds. Moreover, they proposed synthesizing the polymer matrix from biologically derived lactic and glycolic acids. Liu et al. [26] achieved remarkable compressive (428.1 ± 39.7 MPa) and flexural (129.5 ± 13.6 MPa) strengths by utilizing Digital Light Processing (DLP). By adding photocurable resins in the range of 15–30 wt% to regolith, they created a slurry UV-curable formulation, proving it highly effective in creating high-resolution parts and components but unsuitable for producing larger structures.

Thermoplastics have shown promise as binders for lunar regolith. One such approach [27] involves creating filaments to be used in a Fused Filament Fabrication (FFF) machine to create custom parts. The potential of customizing production through such a straightforward process is promising. In addition, such composite material proved to be recyclable. However, a high amount of organic phase (above 60 wt%) is required to maintain the filament ductile enough to feed the system. Efforts to increase the regolith content resulted in a significant increase in brittleness, leading to premature failures. Reducing the amount of additive is achievable by following methods similar to that of polymeric cement. Chen et al. [28] demonstrated that bonding regolith simulant particles is possible with a small amount of binder. The authors combined polyethylene (PE) and JSC-1A, both in powder form, heated them until the polymer melted, and mixed them again. Flexural strength could be enhanced through a two-step grain size gradation, using a weight ratio of 765 : 235 of 90–112 μm and 20–25 μm particles, respectively. They obtained flexural strengths in the same order of magnitude as Portland cement (5 MPa) with just 10 wt% PE. They significantly improved the flexural strength by switching to unsaturated polyester resins (UPR) and introducing a compaction step before

curing [29]. The process began by saturating JSC-1A grains with 15 wt% in UPR. The compaction removed some of the organic phase; the final material had a UPR content ranging from 12.5 wt% (30 MPa applied) to 8.5 wt% (350 MPa applied), with no notable impact on the flexural strength (in the range of 30–40 MPa). Similar results were obtained with epoxy resins [30]. Thermosets are promising but have limited UV radiation resistance [31]. Advanced thermoplastics demonstrated superior UV resistance to epoxy and UPR [32]. In addition, they are recyclable [33]: crushing, remelting, and remolding old parts into new components makes them a sustainable and practical solution for space endeavors. Due to this, advanced thermoplastics were considered, and the benefits of the compaction step in the process were evaluated [34]. By adding 4–6 wt% of thermoplastic and applying a compaction pressure of 100 MPa, the flexural strength could reach up to 14 MPa. With 350 MPa, the strength could even reach 20 MPa. The compaction process came right after mixing the powders and lasted 1 h. All those examples are promising, as they demonstrate that maximizing the utilization of local resources is possible. However, when considering its practical application to real-sized components, the scale and practicality of such an implementation present certain obstacles to address. One challenge in manufacturing real-sized components is high-pressure compaction, which would require impractical levels of force to apply.¹

1.1 Bricks to enable sustainable construction

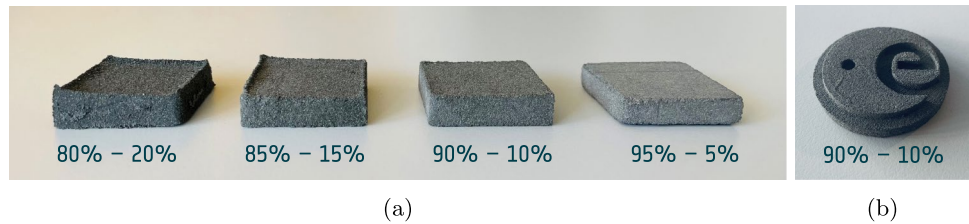
When it comes to construction, the focus is on habitats, landing pads, roads, shelters, and so on: big structures requiring a significant amount of material to handle, process, and assemble. Using local resources is essential but not the only factor to consider; scalability is also crucial. Besides mechanical properties, a reasonable trade-off among operational complexities, robustness, and consumables is required to turn a technology into a payload concept. Standardized structural elements offer several advantages in this respect. They ensure consistency and uniformity, allowing for precise and predictable construction, enabling fine-tuning and optimizing the manufacturing process. Bricks are known for their durability and longevity; brick structures typically require minimal maintenance, reducing long-term costs and ensuring longevity. They provide excellent structural strength and stability, withstanding compressive forces and distributing loads effectively. These aspects made them popular for various construction projects continuing through millennia. Brick-based structures may be easier to set up in early colonization stages. Matter for reflection is given by the multiple examples of self-supporting/free-standing structures that do not require temporary structures during construction (e.g., Nubian vault). In addition, interlocking shapes can replace the use of mortar, promote ease of assembly, and offer design flexibility. Bricks used in construction projects on Earth have different dimensions, depending on the code followed [35]. British codes provide a standardized size (215 × 102.5 × 65 mm) [36], suggesting a possible order of magnitude for lunar bricks by analogy. As discussed, potential high-pressure compaction processes may be challenging to implement in practice with such dimensions involved. This paper aims to demonstrate the potential of a dry aggregate bonding process for producing standardized construction elements. The discussion will outline the steps and optimize process parameters for critical mechanical properties in construction. The results will prove the process can deliver adequate mechanical properties, with minimal and basic steps, simple process requirements, and limiting the amount of Earth-supplied material.

2 The manufacturing process

The process aims to create a composite material in which an organic phase acts as a binder for the regolith. Dry processing of the raw materials offers a key advantage over wet methods in a context where keeping the regolith content high is crucial. Mixing a low amount of liquid binder with a primary and powdery phase creates a sandy/highly viscous mixture. To make it flow through gaps, prolonged mixing and high pressures are needed. Blending the two phases becomes easier when the binder is also in powder form; provided that the grain size dimensions of the two phases are compatible, a uniform blend is possible through mechanical mixing. Thermoplastics enable a dry process; the activities involved PLA powder (Polylactic acid - Axalta Coathylene GC2561) as it is a handy resource for preliminary testing and EAC-1A, the regolith simulant used at the European Astronaut Centre (EAC). The PLA powder

¹ Compacting a small cylinder of 20 mm in diameter with 350 MPa already requires more than 100 kN.

Fig. 1 Preliminary manufacturing campaign: samples with a different content in EAC-1A – PLA. The samples in **a** are 50 × 50 mm size square; the ESA logo in **b** is 60 mm in diameter



had an average particle size of 55–80 μm (90 μm max); the chemical composition and granulometric distribution of EAC-1A are reported in [37].

A set of preliminary samples was initially manufactured, keeping the original granulometric size distribution of EAC-1A and PLA. After manually mixing the powders in a beaker for 2 min, the compound was transferred to a square steel mold (coupons of Fig. 1a) and to a custom silicon mold (coupon of Fig. 1b) and compressed using a toggle press. Lastly, the specimens were baked in an oven at 220 °C for 20 min and cooled in a standard atmosphere. The samples in Fig. 1 have the same weight but a different weight percentage in the two phases. They represent a proof of concept for the process, demonstrating that, as structured, it can produce solid parts with a binder content of 5–20 wt%. Each specimen has unique characteristics due to the varying amounts of organic phase content. The volume of the samples decreases with PLA due to the significant difference in density between the phases. Interestingly, an increase in PLA content results in darker samples. A possible explanation lies in the similar behavior shown by wet sand, as a higher binder content leads to an improved wetting of the inorganic grains. Additionally, as the PLA content increases, the shape of the coupons worsens, particularly on top and lateral surfaces, with noticeable shrinkage. At the same time, coupons with less PLA have blunt edges; the reduced cohesion within the part causes finer details to detach from the samples during mold extraction and manipulation. In parallel, Fig. 1b shows a coupon featuring sharp angles, small pockets, and thin surfaces, proof of concept for the level of detail achievable with the process.

2.1 Detailed process description

This section analyzes the steps involved in the process to gain deeper insights into its mechanisms and highlight the process parameters that might influence the outcome.

2.1.1 Drying

Controlling moisture content before manufacturing is crucial to mitigate variations from the excavation site (EAC-1A) and storage conditions (EAC-1A and PLA). Furthermore, drying is a well-established practice in PLA processing due to its non-negligible moisture absorption [38]. The two phases were individually dried in an air oven; the EAC-1A dried at 250 °C for 2 h, while the PLA at 50 °C for 12 h.

2.1.2 Sieving

Previous research [28] has emphasized the significance of particle size and distribution in regolith. Also, the particle size distribution is known to affect the mechanical properties of the cement [39]. Manual sieves with different mesh sizes were used for sieving. The analysis was conducted at a high level; it only considered grains below specific mesh sizes without combining particles from different sieve fractions.

2.1.3 Weighting and blending

PLA and EAC-1A were weighed separately to achieve the desired weight percentages. The two phases were blended in a beaker using a laboratory spoon for 2 min to reach a thorough mix, promoting good interfacial interaction between the organic and inorganic phases in the following steps.

2.1.4 Mold filling

The mixture was transferred to a metallic mold, giving shape to the part. The internal surfaces needed pre-treatment to limit the adhesion of the organic phase. Applying Kapton tape or a PTFE spray were both found to be effective alternatives. Initial samples showed a significant correlation between even mold filling and the final shape of the part, as the powders have limited flowability even under pressure. A spatula was then used to distribute and level the powder mixture after filling.

2.1.5 Compaction

The mixture was compacted in the mold using a toggle press outfitted with a 2 kN load sensor. Through an Arduino system, real-time force measurements provided control over compaction, ensuring the reproducibility of the results.

2.1.6 Curing

The mold was heated in an oven above the melting temperature of the organic phase, and held for a short time to ensure an even temperature distribution.

2.1.7 Cool down

The mixture was cooled down, allowing the organic phase to solidify. As the organic phase hardened, the part consolidated and strengthened.

3 Process optimization

Process variables can significantly impact the end result. The preliminary samples were manufactured using an arbitrary selection of process parameters, as the objective was to demonstrate the process's feasibility. Specific process outputs must be monitored to understand how variables affect the outcome. Compressive and flexural strength are standard parameters for evaluating materials' performance in civil engineering, as most structural elements undergo compressive and flexural loads. Furthermore, flexural properties offer valuable insights into the material's tensile behavior, albeit to a partial extent. Designs of Experiment (DoE) are systematic methods employed to investigate (and optimize) the effects of multiple variables on a given process or system [40]. They involve designing a set of experiments or tests to analyze the relationship between the input variables (factors) and the output responses. However, when multiple parameters govern a process, employing a full-factorial DoE can potentially result in a substantial number of samples and measurements. The Taguchi approach addresses this issue; it minimizes the impact of variations in input variables and their interactions by employing orthogonal combinations (arrays). Through them, it allows the identification of influential factors and their optimal levels with fewer trials.

3.1 DoE parameters selection

Most process steps are governed by some parameters potentially influencing the mechanical behavior of the parts. Those variables were analyzed to determine which ones could be controlled and measured within the limitation of the experimental setup and rank their role. The main focus areas were the binder weight percentage and the maximum particle size. The significance of the first is well understood, and the impact of particle size distribution in other powdery construction materials is recognized. Four levels were considered for both parameters to assess a possible trend. Then, four other parameters were identified: compaction pressure, curing temperature, curing time, and cooling speed, with two levels each. The number of levels is intentional because an L16 Taguchi design allows for combining factors in this way. Table 1 lists the parameters and their respective levels; Table 2 combines them into the L16 design.

Table 1 Design of Experiment factors and respective levels

Level	Organic phase wt%	Grain size distribution	Compaction pressure ^a	Curing temp.	Curing time	Cooling speed
	F.1	F.2	F.3	F.4	F.5	F.6
1	5	ASR - as received	0.05/0.50 MPa	200 °C	20 min	FAST - air
2	10	< 500 μm	0.50/5.00 MPa	240 °C	40 min	SLOW - oven
3	15	< 250 μm	–	–	–	–
4	20	< 125 μm	–	–	–	–

^a The experimental setup limited the pressure that could be applied to the samples. The high/low levels of the compaction pressure applied on the bigger specimens (flexural samples) were one order of magnitude less than the corresponding ones used for the smaller samples (compression specimens)

Table 2 L16 Taguchi DoE - orthogonal arrays

	01	02	03	04	05	06	07	08	09	10	11	12	13	14	15	16
F.1	1	1	1	1	2	2	2	2	3	3	3	3	4	4	4	4
F.2	1	2	3	4	1	2	3	4	1	2	3	4	1	2	3	4
F.3	1	1	2	2	1	1	2	2	2	2	1	1	2	2	1	1
F.4	1	1	2	2	2	2	1	1	1	1	2	2	2	2	1	1
F.5	1	1	2	2	2	2	1	1	2	2	1	1	1	1	2	2
F.6	1	2	1	2	1	2	1	2	2	1	2	1	2	1	2	1

4 Mechanical characterization

The nature of the material poses a challenge in directly identifying the appropriate test methods to examine compression and flexural strengths. Inspiration was drawn from the protocols used to study concrete while adapting the dimensions of the specimens and the testing speeds to align with the values utilized in reinforced polymer research.

4.1 Compression tests

For compression, reference was made to ASTM D695 [41] (equivalent to ISO 604), covering reinforced rigid plastics, and to ASTM C39 [42], covering concrete. Cylindrical specimens were manufactured through small molds with nominal dimensions of 14 mm in diameter and 30 mm in length, following the DoE pattern of Table 2. The internal surfaces of the molds were sprayed with a PTFE dry film; indeed, their small dimensions made using Kapton tape impractical. The HI and LO levels of the compaction pressure applied before curing were 5.00 MPa and 0.50 MPa, respectively.

Figure 2 illustrates four sets of representative specimens with different binder content. After manufacturing, each sample was measured in weight, height, and diameter using a digital weight scale and caliper to the nearest 0.01 g / 0.01 mm, with each measurement repeated 4 times and the results averaged. Each specimen underwent compression using a uniaxial force applied parallel to its longitudinal axis and transmitted to its top and bottom surfaces through a pair of flat supports. Compression tests were performed using an Instron 8801 machine with a 10 kN load cell. The machine maintained a constant moving speed of 1.3 mm min⁻¹ [41]. The applied load and the displacement of the moving cross-head were measured at a frequency of 10 Hz. For each specimen, the engineering stress (in MPa) was derived by dividing the applied load (in N) by the initial cross-section dimension (in mm²). The compressive strength of each specimen was evaluated in correspondence with the maximum load it could withstand.

4.2 Bending tests

For bending, reference was made to ASTM D790 [43] (equivalent to ISO 178), covering reinforced rigid plastics, and to ASTM C293, covering concrete. Prism specimens with a rectangular cross-section were manufactured following the DoE pattern reported in Table 2. The mold shown in Fig. 3 was designed on purpose by drawing inspiration from the analogous molds for concrete beams in flexural tests. The nominal dimensions of the internal/rectangular volume

Fig. 2 Representative compression specimens: the manufacturing parameters follow the scheme in Table 2; the nominal dimensions are 14 mm in diameter and 30 mm in length

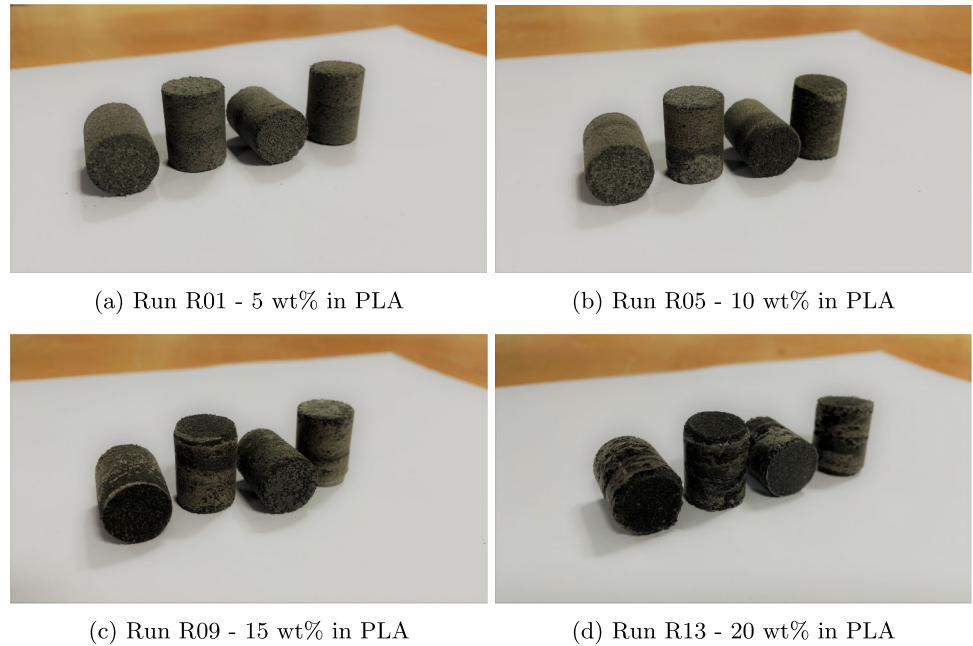
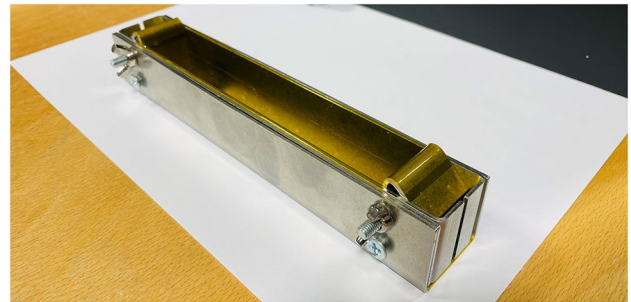


Fig. 3 Steel mold for bending test samples



are 150 mm in length, 25 mm in width, and 25 mm in depth. The internal surfaces were covered in Kapton tape, and the mold was filled with powders up to a depth of 10 mm, manually leveled with a spatula. Given the limitations of the press load cell and the dimensions of the upper surface of the specimens, the HI and LO levels of the compaction pressure applied before curing were lower if compared to the compression samples: 0.50 MPa and 0.05 MPa, respectively. Figure 4 illustrates four sets of representative specimens with different binder content. After manufacturing, the weight and dimensions were evaluated, as done with the previous coupons. Every specimen was bent until failure in a 3-point bending test through three cylindrical supports, two keeping the sample in place (bottom surface - support span of 100 mm) and one loading it on the upper surface. Bending tests were carried out using an Instron 5566A machine with a 500 N load cell. The testing machine maintained a constant speed of 2 mm min⁻¹; this value was determined considering the nominal dimensions of the samples, the support span, and a constant rate of straining of the outer fiber equal to 0.01 mm mm⁻¹ min⁻¹ [43]. The applied load and the displacement of the moving crosshead were measured at a frequency of 10 Hz. The flexural stress was calculated via the applied load (P , in N) and considering the geometry of the specimen through its depth (d), its width (b), and the support span (L) [43], all in mm:

$$\sigma_f = 3PL/2bd^2 \quad (1)$$

Then, the flexural strength of each sample was evaluated in correspondence with the maximum load it could withstand.

Fig. 4 Representative bending specimens: the manufacturing parameters follow the scheme in Table 2; the nominal dimensions are 150 mm in length, 25 mm in width, and 25 mm in depth

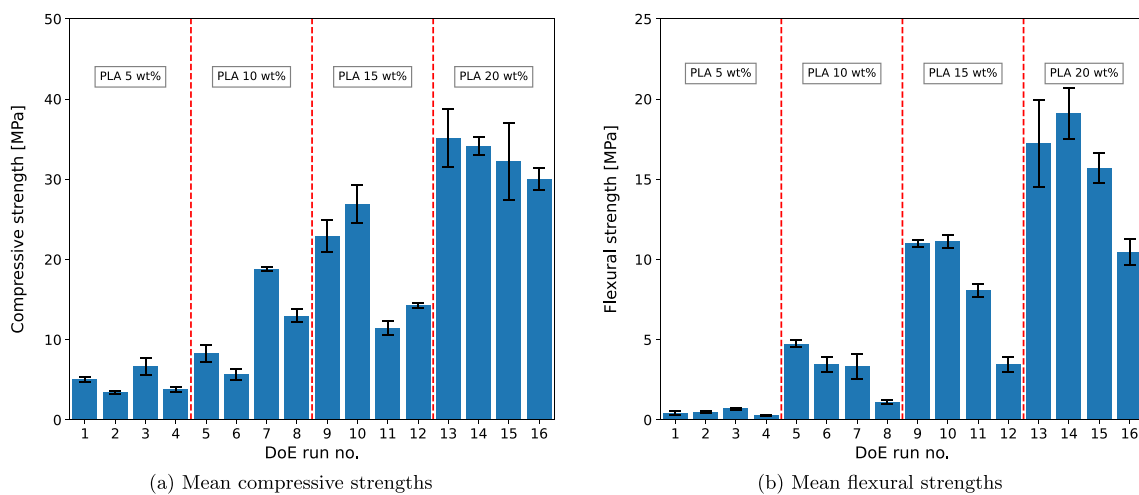
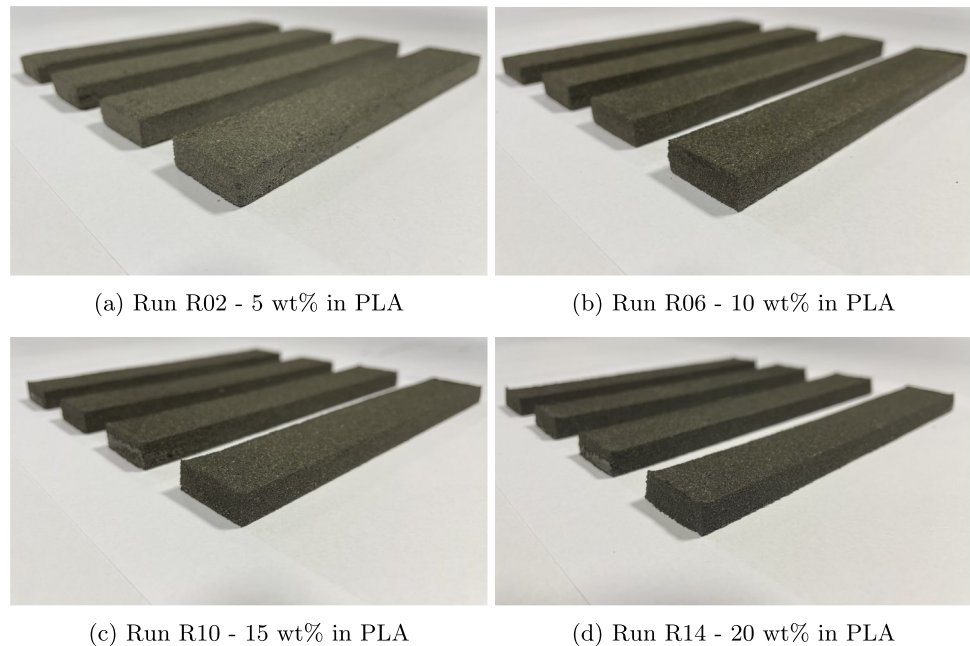


Fig. 5 Summary of experimental results: compression and flexural strengths per each run of the DoE

5 Discussion

Figure 5 summarizes the compression (Fig. 5a) and flexural (Fig. 5b) strengths across both samples. The blue bars indicate the average value per run, while the error bars represent the standard deviation. Both samples show significant variability; compressive strength ranges from 3.40 to 35.2 MPa, and flexural strength from 0.43 to 19.1 MPa. This occurrence is due to the varying combinations of process parameters used for each run. Still, an immediate observation can be made about the binder, as its content positively affects both strengths. For both mechanical characteristics, the experimental campaign focused on determining which factors led to higher strengths, that is, maximizing the quality characteristics. In the postprocessing, the "larger-the-better" *S/N* ratio analysis was used to provide insight into the performance variation caused by the design parameters. The noise factors were considered by performing four times the experiment, that is, having four samples per run of the DoE. The *S/N* ratio was then calculated using the observed data and analyzed to identify the parameter levels optimizing the strengths. To help visualize the main effects of individual factors, Figs. 6 and 7 show the main effects plot on compression and flexural

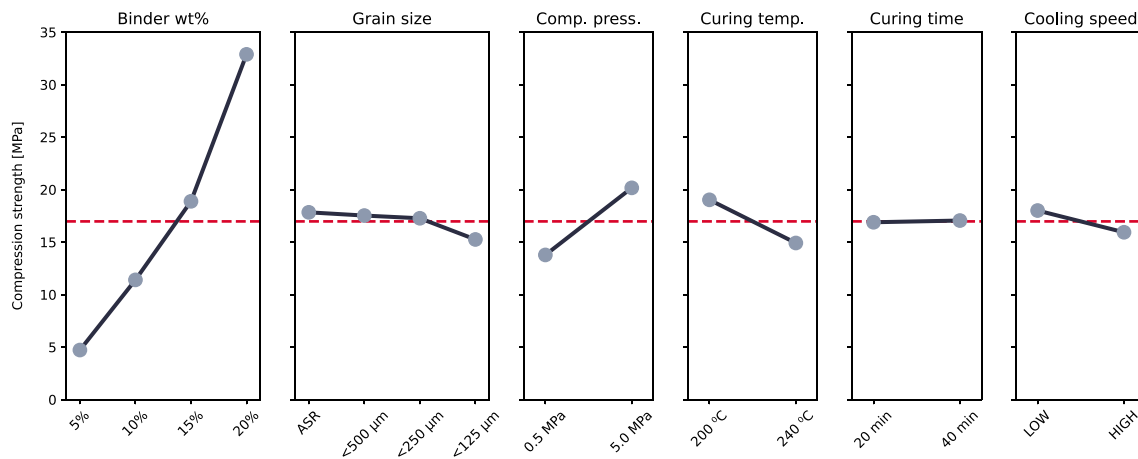


Fig. 6 Compressive strength: main effects plot for means

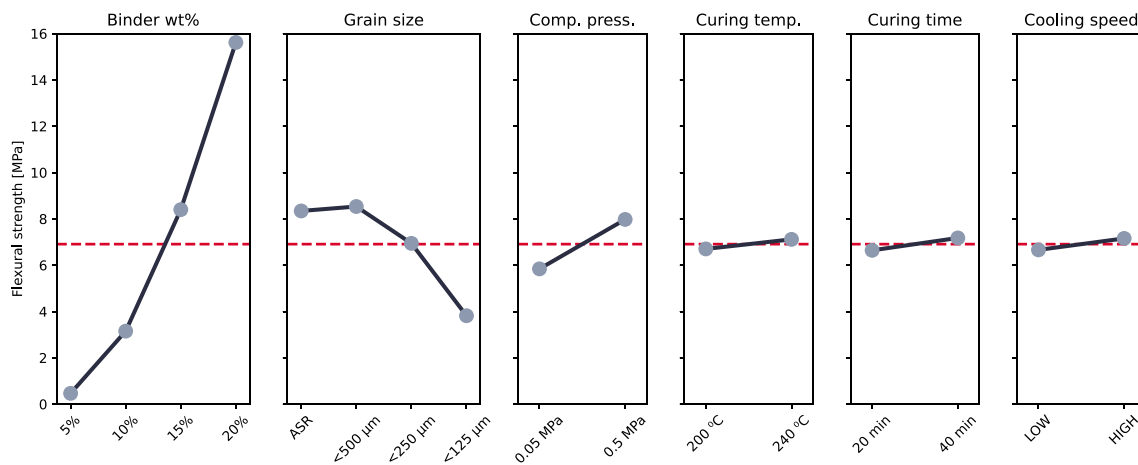


Fig. 7 Flexural strength: main effects plot for means

strength, respectively. They display the average response values for different levels of each control factor, allowing the independent analysis and comparison of the impact of each parameter on the response variable. The response variables (compression and flexural strengths) are on the vertical axis; the levels of the control factors are on the horizontal axis. In both cases, the predominant effect of the binder wt% is confirmed. Adjusting this parameter makes it possible to move across a broad range of compression and flexural strengths. This effect is not unexpected as it is the main responsible for load transmission in the samples. The second plot reveals the role played by grain size distribution. Though with differing intensity, it has a consistent effect that is more pronounced on flexural than compressive strength. Using only the finest fraction leads to a decay of mechanical properties, as this realistically increases the surface area of the grains to wet by the binder. On the other hand, a more heterogeneous particle size distribution reduces such surface area and allows smaller particles to occupy the voids left between larger particles, which is consistent with the observations in [28]. The third plot shows that powder compaction positively affects both strengths, although dissimilar pressure levels were considered. Overall, the other parameters, curing temperature, curing time, and cooling speed, do not appear to play a significant role in the process, despite the difference obtained in compression and bending for the first one. This outcome suggests that it is sufficient to ensure that the interior of the sample reaches the temperature to melt the polymer component. Longer times and higher temperatures do not provide any additional benefit. Additionally, a more rapid cooling is adequate and leads to the development of appropriate strength.

Table 3 Compressive strength: comparison between specific minimum reference requirements for bricks and the experimental data from DoE. C stands for Compliant, C* for Compliant on the Moon (requirements scaled to 1/6), and N for Non-compliant

Ref. standard	cat.	min. [MPa]	RUN															
			01	02	03	04	05	06	07	08	09	10	11	12	13	14	15	16
IBC [44]	-	10.3	C*	C*	C*	C*	C*	C*	C	C	C	C	C	C	C	C	C	
ASTM C410 ^a [45]	T/H	6.9	C*	C*	C	C*	C	C*	C	C	C	C	C	C	C	C	C	
	M/L	13.8	C*	C*	C*	C*	C*	C*	C	C*	C	C	C*	C	C	C	C	
ASTM C62 ^b [46]	NW	10.3	C*	C*	C*	C*	C*	C*	C	C	C	C	C	C	C	C	C	
	MW	17.2	C*	C*	C*	C*	C*	C*	C	C*	C	C	C*	C*	C	C	C	
	SW	20.7	C*	N	C*	C*	C*	C*	C*	C*	C	C	C*	C*	C	C	C	
ASTM C652 ^c [47]	MW	17.2	C*	C*	C*	C*	C*	C*	C	C*	C	C	C*	C*	C	C	C	
	SW	20.7	C*	N	C*	C*	C*	C*	C*	C*	C	C	C*	C*	C	C	C	
ASTM C902 ^d [48]	MX/NX	20.7	C*	N	C*	C*	C*	C*	C*	C*	C	C	C*	C*	C	C	C	
	SX	55.2	N	N	N	N	N	N	N	C*	C*	C*	C*	C*	C*	C*	C*	

^a Industrial Floor Brick

^b Building Brick

^c Hollow Brick

^d Pedestrian and Light Traffic Paving Brick

5.1 Standards for bricks classification

The results highlighted the parameters optimizing compressive and flexural strengths and provided valuable information about achievable strength levels. The behavior of construction materials on Earth has been extensively studied; several standards define the expected compressive strength of bricks based on their intended usage [44–48]. Furthermore, some references give an idea of the strengths required for different concrete construction, even though construction plans and specifications govern them [49]. Staying on concretes, it is also possible to analyze data from various experimental campaigns conducted on different classes to understand their behavior under bending [50–53]. It is widely accepted [54–57] that the requirements in terms of strengths for concrete-based constructions on the Moon would be 1/6 of those of a similar structure on Earth. This reduction factor helps determine initial requirements and evaluate if some of the experimental runs are compliant or equivalent to materials in use on Earth when applied on the Moon. Table 3 reports the minimum brick compressive strengths required on Earth in different applications. These requirements are compared with the results of the experimental campaign. C - Compliant - indicates meeting or exceeding the Earth’s performance requirements, while C* indicates meeting or exceeding the Moon’s performance requirements (1/6 of those on Earth). NC indicates that the results were inadequate for both Earth and Moon applications. Table 4 focuses on concrete. Strength requirements based on the type of construction are listed. The symbols used are consistent with the previous comparison. Table 5 follows a slightly different approach regarding flexural strength. The comparison is with the typical values measured on different types of concretes. Runs performing equivalently or better than the concrete being considered are classified as E - Equivalent. Equivalent on the Moon (E*) and Non Equivalent (N) have clear meanings. The comparisons show that the performances obtained are promising in both perspectives. Most of the runs with the highest content in the organic phase even met the strict requirements on Earth. When the regolith content grows, the performances decline, but compliance with the compression requirements on the Moon is guaranteed in most cases. A separate discussion involves flexural strength, as the runs with the lowest amount of PLA (5 wt%) did not reach expectations. Notably, the pressure levels used for powder compaction were one order of magnitude lower than those used for compression specimens. It’s reasonable to expect improvements in performance with coherent pressure levels.

Table 4 Compressive strength: comparison between specific minimum reference requirements for concretes, based on the construction, and the experimental data from DoE. C stands for Compliant, C* for Compliant on the Moon (requirements scaled to 1/6), and N for Non-compliant

	exp. val. [MPa]	RUN															
		01	02	03	04	05	06	07	08	09	10	11	12	13	14	15	16
[49]	(< 17) ^a	C	C	C	C	C	C	C	C	C	C	C	C	C	C	C	C
	(17 – 24) ^b	C*	C*	C*	C*	C*	C*	C*	C*	C	C	C*	C*	C	C	C	C
	(21 – 28) ^c	C*	C*	C*	C*	C*	C*	C*	C*	C	C	C*	C*	C	C	C	C
	(21 – 48) ^d	C*	C*	C*	C*	C*	C*	C*	C*	C	C	C*	C*	C	C	C	C
	(28 – 48) ^e	C*	N	C*	N	C*	C*	C*	C*	C	C	C*	C*	C	C	C	C
	(69 – 109) ^f	N	N	N	N	N	N	C*	C*	C*	C*	N	C*	C*	C*	C*	C*

- ^a Concrete fill
- ^b Basement and foundation walls and slabs, walks, patios, steps and stairs
- ^c Driveways, garage and industrial floor slabs
- ^d Reinforced concrete beams, slabs, columns and walls
- ^e Precast and prestressed concrete
- ^f High-rise buildings (columns)

Table 5 Flexural strength / modulus of rupture: comparison between the experimental values of different concretes and the experimental data from DoE. E stands for Equivalent (or superior), E* for Equivalent on the Moon (or superior - requirements scaled to 1/6), and N for Non-equivalent

	Grade	exp. value(s) [MPa]	RUN															
			01	02	03	04	05	06	07	08	09	10	11	12	13	14	15	16
[50] ^a	20 MPa	3.5	N	N	E*	N	E	E*	E*	E*	E	E	E	E*	E	E	E	E
	35 MPa	5.2 – 7.6	N	N	N	N	E*	E*	E*	E*	E	E	E	E*	E	E	E	E
	65 MPa	7.2 – 10	N	N	N	N	E*	E*	E*	N	E	E	E	E*	E	E	E	E
[51] ^b	85 MPa	8.0 – 11	N	N	N	N	E*	E*	E*	N	E	E	E	E*	E	E	E	E
	NWHS ^c	6.9	N	N	N	N	E*	E*	E*	N	E	E	E	E*	E	E	E	E
	LWplain ^d	4.4	N	N	N	N	E	E*	E*	E*	E	E	E	E*	E	E	E	E
	LWP ^e	4.6 – 5.3	N	N	N	N	E	E*	E*	E*	E	E	E	E*	E	E	E	E
[52] ^f	LWS ^f	5.2 – 7.9	N	N	N	N	E*	E*	E*	E*	E	E	E	E*	E	E	E	E
	0.5 %vol	8.2	N	N	N	N	E*	E*	E*	N	E	E	E*	E*	E	E	E	E
	1.0 %vol	10.1	N	N	N	N	E*	E*	E*	N	E	E	E*	E*	E	E	E	E
	1.5 %vol	12.3	N	N	N	N	E*	E*	E*	N	E*	E*	E*	E*	E	E	E	E*
	2.0 %vol	14.5	N	N	N	N	E*	E*	E*	N	E*	E*	E*	E*	E	E	E	E*

- ^a Standard Concrete
- ^b Steel Fiber-Reinforced Concrete
- ^c Normal Weight High-Strength Concrete
- ^d Plain Lightweight Concrete
- ^e Steel Fiber-Reinforced Lightweight Concrete
- ^f Polypropilene Fiber-Reinforced Lightweight Concrete
- ^g High-Strength Steel Fiber-Reinforced Concrete

6 Conclusion

This study focused on regolith-based composites using low amounts of thermoplastic binders. PLA was considered to evaluate the feasibility of the manufacturing process. The regolith grains and binder powders are compacted in a mold. Then, the mixture is cured: the temperature is increased and kept constant until the binder phase melts. During

cooling, the organic phase solidifies, and the part strengthens. Six process parameters were evaluated in an L16 DoE for their impact on compressive and flexural strengths. Unsurprisingly, increasing the amount of binder improved both properties. However, they also improved by increasing compaction and using a heterogeneous particle size distribution.

The process proved the capability of manufacturing components standardized in shape having mechanical properties compatible with or exceeding possible requirements for construction on the Moon, even with minimal binder and low compaction pressure, allowing for easy scalability to larger-sized end products. With only 5 wt% binder, the compressive strength requirements for bricks in industrial floors, buildings, and pedestrian/light traffic paving on the Moon were met and exceeded. 10 wt% binder already allowed to meet the requirements of structures on Earth. Similarly, the compressive strength requirements set for concrete would be met on the Moon with only 5 wt% binder in most constructions, including basement and foundation walls and slabs and reinforced concrete beams, slabs, columns, and walls. The results were less explicit when it comes to flexural strength. Despite the setup limiting the compaction pressure on bigger samples, the equivalent performances of standard concrete were met with 5 wt% of binder and those of high-strength concrete with 10 wt%.

This study is important to in-situ resource utilization, specifically for large-scale surface constructions and infrastructures. It shows that it is possible to meet the necessary performance criteria without overly demanding processes. Future studies will transfer this capability to advanced thermoplastic, properly characterize the entire spectrum of mechanical properties with the optimum parameters and evaluate temperature effects and radiation resistance.

Author contributions All authors contributed to the study conception and design. Material preparation was performed by RT. Data collection and analysis were performed by RT and CGF. Conceptualization and supervision were provided by RT and AC. The first draft of the manuscript was written by RT, and all authors commented on previous versions of the manuscript. All authors read and approved the final manuscript.

Funding This research received no external funding.

Data availability The raw data supporting the findings of this study are available in the NOMAD repository with the identifier [jl4Vlp-4Sx2jFBlv2x_sgQ](https://doi.org/10.26434/chemrxiv-2024-jl4vl)

Declarations

Competing interests The authors declare no competing interests.

Open Access This article is licensed under a Creative Commons Attribution 4.0 International License, which permits use, sharing, adaptation, distribution and reproduction in any medium or format, as long as you give appropriate credit to the original author(s) and the source, provide a link to the Creative Commons licence, and indicate if changes were made. The images or other third party material in this article are included in the article's Creative Commons licence, unless indicated otherwise in a credit line to the material. If material is not included in the article's Creative Commons licence and your intended use is not permitted by statutory regulation or exceeds the permitted use, you will need to obtain permission directly from the copyright holder. To view a copy of this licence, visit <http://creativecommons.org/licenses/by/4.0/>.

Appendix A

Figure 8 shows magnified surface pictures for a representative flexural sample per run. All images are arranged with decreasing particle size from left to right and increasing organic content from top to bottom. Run 09 gives a clear example, showing particles larger than 500 μm , with a big whitish grain being noticeable. At the same time, the last column clearly indicates that the powders are finer. The different content in the organic phase is less visible; however, the specimens of the last row exhibit glassy and shiny surfaces, indicating a higher concentration of PLA. The observation made on the outer specimens' color is confirmed, as there is a gradual increase in the darker shades while moving from the top down. The combination of the other four process parameters is less trivial. The figures also highlight distributed porosity. Voids are present in all specimens, and the off-focus regions reveal the layers beneath. In addition, the regolith grains demonstrate a heterogeneous mixing of different minerals.

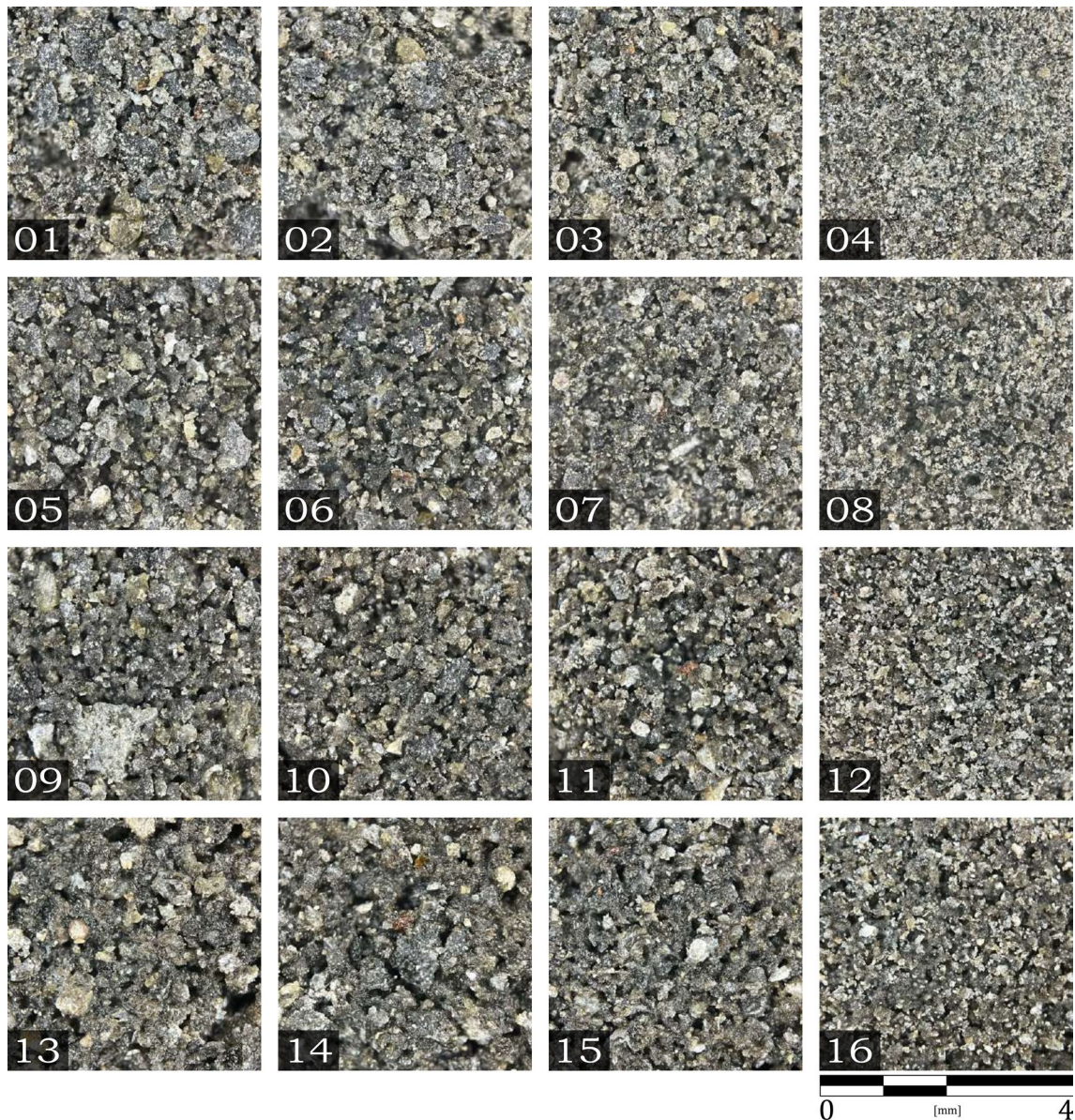


Fig. 8 Magnified surface pictures of a representative flexural sample per run

References

1. Vallerani E, Ori G-G, Torre A, Grasso M, Guizzo GP, Vukman I. Isru: perspectives for lunar development. In: 57th International Astronautical Congress, 2006: 1–15. <https://doi.org/10.2514/6.IAC-06-A5.1.04>
2. Tilman S, Doris B, Torrence VJ. The encyclopedia of the solar system. Amsterdam, NL: Elsevier; 2014. <https://doi.org/10.1016/C2010-0-67309-3>.
3. NASA: NASA's moon to mars strategy and objectives development (2022). <https://go.nasa.gov/3zzSNhp> Accessed 04 Oct 2023
4. Anand M, Crawford I, Balat-Pichelin M, Abanades S, Westrenen W, Péraudeau G, Jaumann R, Seboldt W. A brief review of chemical and mineralogical resources on the moon and likely initial in situ resource utilization (isru) applications. Planet Space Sci. 2012;74:42–8. <https://doi.org/10.1016/j.pss.2012.08.012>.
5. McKay DS, Heiken G, Basu A, Blanford G, Simon S, Reedy R, French BM, Papike J. Lunar sourcebook: a user's guide to the moon. New York: Cambridge University Press; 1991.
6. Cannon KM, Mueller RP, Badescu V, Zacny K, Bar-Cohen Y. Regolith processing. Cham: Springer; 2023. p. 399–427.
7. Lomax B, Conti M, Khan N, Bennett N, Ganin A, Symes M. Proving the viability of an electrochemical process for the simultaneous extraction of oxygen and production of metal alloys from lunar regolith. Planet Space Sci. 2019;180: 104748. <https://doi.org/10.1016/j.pss.2019.104748>.

8. Sowers G, Dreyer C. Ice mining in lunar permanently shadowed regions. *New Space*. 2019;7:1–10. <https://doi.org/10.1089/space.2019.0002>.
9. Rich B, Lökk H, Arnhof M, Cheibas I. Advanced concepts for isru-based additive manufacturing of planetary habitats. In: 16th European Conference on Spacecraft Structures, Materials and Environmental Testing (ECSSMET 2021). 2021; 1–13. <https://doi.org/10.6084/m9.figshare.14345537.v1>
10. Karl D, Cannon K, Gurlo A. Review of space resources processing for mars missions: Martian simulants, regolith bonding concepts and additive manufacturing. *Open Ceram*. 2021;9: 100216. <https://doi.org/10.1016/j.oceram.2021.100216>.
11. Farries KW, Visintin P, Smith ST, Eyk P. Sintered or melted regolith for lunar construction: state-of-the-art review and future research directions. *Constr Build Mater*. 2021;296: 123627. <https://doi.org/10.1016/j.conbuildmat.2021.123627>.
12. Han W, Ding L, Cai L, Zhu J, Luo H, Tang T. Sintering of hust-1 lunar regolith simulant. *Constr Build Mater*. 2022;324: 126655. <https://doi.org/10.1016/j.conbuildmat.2022.126655>.
13. Fateri M, Meurisse A, Sperl M, Urbina D, Madakashira H, Govindaraj S, Gancet J, Imhof B, Hoheneder W, Waclavicek R, Preisinger C, Podreka E, Makthoum M, Weiss P. Solar sintering for lunar additive manufacturing. *J Aerosp Eng*. 2019;32:04019101. [https://doi.org/10.1061/\(ASCE\)AS.1943-5525.0001093](https://doi.org/10.1061/(ASCE)AS.1943-5525.0001093).
14. Thiébaud L, Cowley A. Microwave processing of regolith - a 1d-printing cavity for enabling lunar construction technology. In: 8th European Conference for Aeronautics and Space Sciences (EUCASS). 2019; 1–13. <https://doi.org/10.13009/EUCASS2019-917>
15. Imhof B, Urbina D, Weiss P, Sperl M, Hoheneder W, Waclavicek R, Madakashira H, Salini J, Govindaraj S, Gancet J, Makthoum M, Gobert T, Fateri M, Meurisse A, D'Angelo O, Preisinger C. Advancing solar sintering for building a base on the moon. In: 68th International Astronautical Congress. 2017; 1–17
16. Lim S, Bowen J, Degli-Alessandrini G, Anand M, Cowley A, Prabhu V. Investigating the microwave heating behaviour of lunar soil simulant jsc-1a at different input powers. *Sci Rep*. 2021;11:2133. <https://doi.org/10.1038/s41598-021-81691-w>.
17. Meurisse A, Beltzung J, Kolbe M, Cowley A, Sperl M. Influence of mineral composition on sintering lunar regolith. *J Aerosp Eng*. 2017;30:04017014. [https://doi.org/10.1061/\(ASCE\)AS.1943-5525.0000721](https://doi.org/10.1061/(ASCE)AS.1943-5525.0000721).
18. Warren P, Raju N, Ebrahimi H, Krzmanovic M, Raghavan S, Kapat J, Ghosh R. Effect of sintering temperature on microstructure and mechanical properties of molded Martian and lunar regolith. *Ceram Int*. 2022;48:35825–33. <https://doi.org/10.1016/j.ceramint.2022.07.329>.
19. Khoshnevis B, Bodiford M, Burks K, Ethridge E, Tucker D, Kim W, Toutanji H, Fiske M. Lunar contour crafting: a novel technique for isru-based habitat development. In: 43rd AIAA Aerospace Sciences Meeting and Exhibit - Meeting Papers. 2005; 1–13. <https://doi.org/10.2514/6.2005-538>
20. Mueller RP, Townsend II, Tamasy GJ, Evers CJ, Sibille LJ, Edmunson JE, Fiske MR, Fikes JC, Case MP. Additive construction with mobile emplacement (acme)/automated construction of expeditionary structures (aces) materials delivery system (mds). In: 16th Biennial International Conference on Engineering, Science, Construction, and Operations in Challenging Environments. 2018; 193–206. <https://doi.org/10.1061/9780784481899.020>
21. Davis G, Montes C, Eklund S. Preparation of lunar regolith based geopolymer cement under heat and vacuum. *Adv Space Res*. 2017;59(7):1872–85. <https://doi.org/10.1016/j.asr.2017.01.024>.
22. Ceccanti F, Dini E, De Kestelier X, Colla V, Pambaguian L. 3d printing technology for a moon outpost exploiting lunar soil. In: 61st International Astronautical Congress. 2010; 1–9
23. Cesaretti G, Enrico D, De Kestelier X, Colla V, Pambaguian L. Building components for an outpost on the lunar soil by means of a novel 3d printing technology. *Acta Astronautica*. 2014;93:430–50. <https://doi.org/10.1016/j.actaastro.2013.07.034>.
24. Taylor S, Jakus A, Koube K, Ibeh A, Geisendorfer N, Shah R, Dunand D. Sintering of micro-trusses created by extrusion-3d-printing of lunar regolith inks. *Acta Astronautica*. 2017;143:1–8. <https://doi.org/10.1016/j.actaastro.2017.11.005>.
25. Jakus A, Koube K, Geisendorfer N, Shah R. Robust and elastic lunar and Martian structures from 3d-printed regolith inks. *Sci Rep*. 2017;7:44931. <https://doi.org/10.1038/srep44931>.
26. Liu M, Weizhe T, Duan W, Li S, Dou R, Wang G, Liu B, Wang L. Digital light processing of lunar regolith structures with high mechanical properties. *Ceram Int*. 2018;45:5829–36. <https://doi.org/10.1016/j.ceramint.2018.12.049>.
27. Pichard P-L, Cowley A, Hand A, Schild T, Adiaconitei A, Katrakova-Kruger D, Spanheimer V, Ochsner: Regolith-based composite manufacturing by fused deposition modelling (fdm). In: *Space Resources Week*. 2022.
28. Chen T, Chow B, Wang M, Shi Y, Zhao C, Qiao Y. Inorganic-organic hybrid of lunar soil simulant and polyethylene. *J Mater Civ Eng*. 2015;28:06015013. [https://doi.org/10.1061/\(ASCE\)MT.1943-5533.0001450](https://doi.org/10.1061/(ASCE)MT.1943-5533.0001450).
29. Chen T, Chow B, Wang M, Zhong Y, Qiao Y. High-pressure densification of composite lunar cement. *J Mater Civ Eng*. 2017;29:06017013. [https://doi.org/10.1061/\(ASCE\)MT.1943-5533.0002047](https://doi.org/10.1061/(ASCE)MT.1943-5533.0002047).
30. Chen T, Chow B, Zhong Y, Wang M, Kou R, Qiao Y. Formation of polymer micro-agglomerations in ultralow-binder-content composite based on lunar soil simulant. *Adv Space Res*. 2017;61:830–6. <https://doi.org/10.1016/j.asr.2017.10.050>.
31. Armstrong RD, Jenkins A, Johnson BW. An investigation into the uv breakdown of thermoset polyester coatings using impedance spectroscopy. *Corros Sci*. 1995;37:1615–25. [https://doi.org/10.1016/0010-938X\(95\)00063-P](https://doi.org/10.1016/0010-938X(95)00063-P).
32. Alvino W. Ultraviolet stability of polyimides and polyamide-imides. *J Appl Polym Sci*. 1971;15:2123–40. <https://doi.org/10.1002/app.1971.070150907>.
33. Zhu Y, Romain C, Williams C. Sustainable polymers from renewable resources. *Nature*. 2016;540:354–62. <https://doi.org/10.1038/nature21001>.
34. Oh K, Chen T, Kou R, Yi H, Qiao Y. Ultralow-binder-content thermoplastic composites based on lunar soil simulant. *Adv Space Res*. 2020;66:2245–50. <https://doi.org/10.1016/j.asr.2020.07.041>.
35. Murmu A, Patel A. Towards sustainable bricks production : an overview. *J Constr Build Mater*. 2018;165:112–25. <https://doi.org/10.1016/j.conbuildmat.2018.01.038>.
36. Lynch GCJ. Bricks: properties and classifications. *Struc Surv*. 1994;12:15–20. <https://doi.org/10.1108/02630809410066447>.
37. Engelschiøn V, Eriksson S, Cowley A, Fateri M, Meurisse A, Kueppers U, Sperl M. Eac-1a: a novel large-volume lunar regolith simulant. *Sci Rep*. 2020;10:5473. <https://doi.org/10.1038/s41598-020-62312-4>.

38. Lim L-T, Vanyo T, Randall J, Cink K, Agrawal AK. Processing of poly(Lactic Acid). Hoboken: John Wiley & Sons; 2022. p. 231–70.
39. Bentz D, Garboczi EJ, Haecker C, Jensen O. Effects of cement particle size distribution on performance properties of Portland cement-based materials. *Cem Concr Res*. 1999;29:1663–71. [https://doi.org/10.1016/S0008-8846\(99\)00163-5](https://doi.org/10.1016/S0008-8846(99)00163-5).
40. Durakovic B. Design of experiments application, concepts, examples: state of the art. *Period Eng Nat Sci*. 2017;5:421–39. <https://doi.org/10.21533/pen.v5i3.145>.
41. ASTM: Standard D695 - Standard Test Method for Compressive Properties of Rigid Plastics. ASTM International, West Conshohocken, PA. 2015. <https://doi.org/10.1520/D0695-15>
42. ASTM: Standard C39 - Standard Test Method for Compressive Strength of Cylindrical Concrete Specimens. ASTM International, West Conshohocken, PA. 2021. https://doi.org/10.1520/C0039_C0039M-21
43. ASTM: Standard D790 - Standard Test Methods for Flexural Properties of Unreinforced and Reinforced Plastics and Electrical Insulating Materials. ASTM International, West Conshohocken, PA. 2017. <https://doi.org/10.1520/D0790-17>
44. International Building Code. International Code Council, Falls Church, VA, 2020.
45. ASTM: Standard C410 - Standard Specification for Industrial Floor Brick. ASTM International, West Conshohocken, PA. 2017. <https://doi.org/10.1520/C0410-13R17>
46. ASTM: Standard C62 - Standard Specification for Building Brick (Solid Masonry Units Made From Clay or Shale). ASTM International, West Conshohocken, PA. 2017. <https://doi.org/10.1520/C0062-17>
47. ASTM: Standard C652 - Standard Specification for Hollow Brick (Hollow Masonry Units Made From Clay or Shale). ASTM International, West Conshohocken, PA. 2021. <https://doi.org/10.1520/C0652-21>
48. ASTM: Standard C902 - Standard Specification for Pedestrian and Light Traffic Paving Brick. ASTM International, West Conshohocken, PA. 2020. <https://doi.org/10.1520/C0902-20>
49. Neville GB. The concrete manual. Falls Church: International Code Council; 2015.
50. Kumar MVJ. Strength characteristics of self-curing concrete. *Int J Res Eng Technol*. 2012;01:51–7. <https://doi.org/10.15623/ijret.2012.0101007>.
51. Job T, Ananth R. Mechanical properties of steel fiber-reinforced concrete. *J Mater Civ Eng*. 2007;19(5):385–92. [https://doi.org/10.1061/\(ASCE\)0899-1561\(2007\)19:5\(385\)](https://doi.org/10.1061/(ASCE)0899-1561(2007)19:5(385)).
52. Kayali O, Haque MN, Zhu B. Some characteristics of high strength fiber reinforced lightweight aggregate concrete. *Cem Concr Compos*. 2003;25:207–13. [https://doi.org/10.1016/S0958-9465\(02\)00016-1](https://doi.org/10.1016/S0958-9465(02)00016-1).
53. Song PS, Hwang S. Mechanical properties of high-strength steel fiber-reinforced concrete. *Constr Build Mater*. 2004;18:669–73. <https://doi.org/10.1016/j.conbuildmat.2004.04.027>.
54. Benaroya H, Bernold L. Engineering of lunar bases. *Acta Astronautica*. 2008;62:277–99. <https://doi.org/10.1016/j.actaastro.2007.05.001>.
55. Montes C, Broussard K, Gongre M, Simicevic N, Mejia J, Tham J, Allouche E, Davis G. Evaluation of lunar regolith geopolymer binder as a radioactive shielding material for space exploration applications. *Adv Space Res*. 2015;56:1212–21. <https://doi.org/10.1016/j.asr.2015.05.044>.
56. Goulas A, Binner JG, Engström DS, Harris RA, Friel RJ. Mechanical behaviour of additively manufactured lunar regolith simulant components. *Proc Inst Mech Eng Part L J Mater Des Appl*. 2019;233(8):1629–44. <https://doi.org/10.1177/1464420718777932>.
57. Lee S, Riessen A. A review on geopolymer technology for lunar base construction. *Materials*. 2022;15(13):1–11. <https://doi.org/10.3390/ma15134516>.

Publisher's Note Springer Nature remains neutral with regard to jurisdictional claims in published maps and institutional affiliations.